RSC Advances

ROYAL SOCIETY OF CHEMISTRY

www.rsc.org/advances

Journal Name

ARTICLE

Bioinspired Fabrication and Lead Adsorption Property of Nano-hydroxyapatite/Chitosan Porous Materials

Received 00th January 20xx,
Accepted 00th January 20xx

DOI: 10.1039/x0xx00000x

www.rsc.org/

Yong Lei†, Wei Chen†, Bin Lu, Qin-Fei Ke and Ya-Ping Guo*

Both hydroxyapatite (HAP) and chitosan (CS) powders have good adsorption activity for Pb^{2+} ions, but it is difficult to separate the adsorbent powders from wastewaters. Herein, we report the bioinspired fabrication of nano-HAP/CS porous materials (HCPMs) according to the following steps: (i) freeze-drying fabrication of brushite (DCPD)/CS porous materials (BCPMs); and (ii) conversion of HCPMs from BCPMs by alkaline solution treatment. The HCPMs possess interconnected three-dimensional (3D) macropores with a pore size of 150~240 μm and a porosity of 93.0%. The nano-HAP rods with a length of ~500 nm and a diameter of ~20 nm disperse uniformly within the porous materials. As lead aqueous solutions flow through the HCPMs, the Pb^{2+} ions are chemically adsorbed on the adsorbents by forming lead hydroxyapatite (PbHAP, $Pb_{10}(PO_4)_6(OH)_2$) and CS-Pb complex. The conversion mechanism of HAP to PbHAP is a dissolution-precipitation reaction. Notably, the pH values of lead solutions have great effect on the adsorption capacity of the HCPMs. With decreasing the pH values from 7.0 to 2.5, the experimental equilibrium adsorption amount increases from 208.0 to 548.9 mg/g. Adsorption kinetic and adsorption isotherm studies reveal that the adsorption of Pb^{2+} ions on the HCPMs exhibits good compliance with pseudo-second-order kinetic and Langmuir isotherm model. Hence, the HCPMs can be used for the chemical adsorption of Pb^{2+} ions from wastewater.

1. Introduction

Heavy metal ions, primarily originated from anthropogenic activities, pose significant threats to human health even in a very low concentration.[1-3] Among hazardous heavy metal ions, Pb^{2+} ions in aqueous solutions attract special attentions. Pb^{2+} ions not only inhibit enzymes by binding to -SH groups in proteins, but also alter bone cell function by changing the circulating levels of hormones, particularly 1,25-dihydroxyvitamin D_3, and by perturbing the ability of bone cells to respond to hormonal regulation.[4] If excessive inhalation or swallowing, Pb^{2+} ions may cause mental disturbance, retardation, dysfunction of kidneys, brain damage as well as behavioral problems, or even death.[5-8] Therefore, the Pb^{2+} ions in industrial wastewaters must be removed up to a low concentration of 0.05~0.1 mg/L before being released into environment.[9-11]

In the past few decades, several methods have been developed for the removal of toxic heavy metal ions from wastewaters, including chemical precipitation, ion exchange, membrane filtration, solvent extraction, coagulation, phytoextraction, ultrafiltration, electrochemical treatment, reverse osmosis and adsorption.[12-17] However, most of the above technologies have the disadvantages such as poor removal efficiency and high energy requirement, especially for heavy metal ions with low concentrations.[18] Fortunately, adsorption technology is considered as a highly effective, economic, environmentally friendly and easily operational method to remove heavy metals.[1,19] The adsorption process offers a flexible operation, and generally yields high-quality treated effluents. Moreover, adsorbents can be regenerated via suitable desorption processes. Ideal absorbents should possess nontoxicity to environment, and have good sorption capacity for heavy metal ions. The common adsorbents for the removal of Pb^{2+} ions primarily include activated carbons, zeolites, meranti sawdust, clays, sludge-derived biochar, and chitason (CS).[20-23]

Recently, apatite-based mineral materials have become promising adsorbents for the removal of heavy metal ions because of their high chemical activity and biological stability.[24-26] Hydroxyapatite [$Ca_{10}(PO_4)_6(OH)_2$, HAP], a member of apatite mineral family, is well-known as predominant inorganic constituent of natural bones and teeth, and the corresponding synthetic materials exhibit environmental friendly characteristics. Moreover, HAP as a adsorbent for the removal of heavy metal ions from aqueous solutions possesses many advantages including high removal capacity, low water solubility, low cost and high stability under oxidizing or reducing conditions.[27-29] The adsorption mechanisms of HAP for heavy metal ions mainly include ion exchange, dissolution/precipitation, and surface complexes.[30,31] For

The Education Ministry Key Lab of Resource Chemistry and Shanghai Key Laboratory of Rare Earth Functional Materials, Shanghai Normal University, Shanghai 200234, PR China.

† Y. Lei and W. Chen contributed equally to this work.

Electronic Supplementary Information (ESI) available: [details of any supplementary information available should be included here]. See DOI: 10.1039/x0xx00000x

example, the Ca^{2+} ions in HAP crystal lattices can be substituted by other metal ions (Ba^{2+}, Sr^{2+}, Cd^{2+}, Pb^{2+}, Zn^{2+}, Ni^{2+}, Co^{2+}, and Cu^{2+}) via an ion exchange reaction.[31-33] The sorption capacities of HAP for metal cations not only depend on metal ion concentrations, solution pH values, contact time and ionic species, but also are ascribed to the porous structure and crystallinity of HAP. The pores in HAP materials can serve as ion channels, and thus increase ionic exchange and heavy metal immobilization.[30,34] In addition, HAP with low crystallinity possesses many lattice defects, which can serve as active sites to chemically absorb heavy metal ions. Generally, HAP powders are used as adsorbents for the removal of heavy metal ions, but it is difficult to separate HAP powders from wastewaters.[35] Alternatively, HAP porous materials not only effectively remove heavy metals ions under flow conditions, but also can be separated from aqueous solutions. As compared with HAP powders, HAP porous materials are more suitable for industrial application.

As we know, natural bones are hybrid nanostructured collagen-HAP composites with hierarchically porous structures.[36] During the biomineralization of bone minerals, nano-HAP particles are converted from amorphous calcium phosphate (ACP) by using octacalcium phosphate (OCP, $Ca_8H_2(PO_4)_5{\cdot}5H_2O$) and brushite (DCPD, $CaHPO_4{\cdot}2H_2O$) as transitory precursors.[36] Herein, we fabricate nano-HAP/CS porous materials (HCPMs) using brushite/CS porous materials (BCPMs) as precursors.[37-39] The HCPMs have the following advantages: firstly, both HAP and CS are environmental friendly materials; secondly, the HCPMs possess excellent adsorption activity for heavy metal ions; finally, if porous composite materials serve as absorbents, the separation process of heavy metal ions from wastewater is easy and low-cost, even under flow conditions. The main aims of this work are to fabricate HCPMs, to study their morphology, structure and formation mechanism, and to investigate their adsorption performance and kinetics for Pb^{2+} ions under flow conditions.

2. Experimental

2.1 Materials and reagents

Chitosan (90% deacetylated form) was purchased from Richjoint Chemical Reagent Co., Ltd. (Shanghai, China). Acetic acid (Aladdin, 99.9%, AR), calcium nitrate tetrahydrate (Merck, 99.9%, AR), nitric acid (Aladdin, 65%, AR), sodium dihydrogen phosphate dehydrate (Aladdin, 99.9%, AR), sodium hydroxide pellets (Merck GR, 98%), lead nitrate (Aladdin, AR), and absolute ethanol (Richjoint, AR) were of high purity. Deionized water was used throughout the experiment. All the chemicals were used without any further purification.

2.2 Preparation of HCPMs

A homogeneous CS solution (3.85 wt%, 50 ml) was prepared by adding CS powders (2.0 g) into an acetic acid solution (50 ml, 2 vol%). The solution was stirred for 12 h and sonicated for 1 h to remove air bubbles. $Ca(NO_3)_2{\cdot}4H_2O$ (2.3616 g) and $NaH_2PO_4{\cdot}2H_2O$ (0.936 g) were added into the CS solution under agitation. The above mixtures were transferred into 24-well plates and cooled at -20°C in a freezer for 5 h. The samples were rapidly transferred to a freeze-drying machine to deeply freeze at -35~-40°C. The solidified mixtures were subsequently freeze-dried for 42 h. After the freeze-drying process, the BCPMs were treated with a NaOH solution (5 wt%) at 37°C for 3 days. The final products (HCPMs) were washed with deionized water and dried under vacuum dryer. In addition, CPMs and HAP powders served as control samples. The CS porous materials (CPMs) were prepared at the same conditions but without adding $Ca(NO_3)_2{\cdot}4H_2O$ and $NaH_2PO_4{\cdot}2H_2O$. The HAP powders were prepared according to the following procedures. 0.5 M $CaCl_2$ and 0.3 M $(NH_4)_2HPO_4$ were diluted with 250 mL of deionized water, respectively. The $(NH_4)_2HPO_4$ solution was added dropwise into the $CaCl_2$ solution for 30 min at 40°C. The mixed solution was stirred sequentially for 1 h and aged subsequently for 12 h at 40°C. During the precipitation process, the pH value of the above solution was kept at 10.0 by the addition of ammonia. Finally, the product (HAP) was filtered off, washed with distilled water, and dried at 60°C for 2 days.

2.3 Adsorption experimental of Pb^{2+} ions

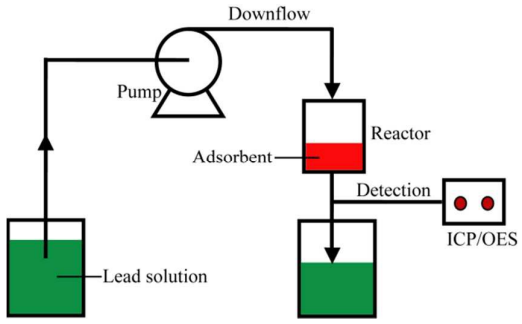

Figure 1. Schematic of the continuous adsorption of Pb^{2+} ions on adsorbents.

The adsorption experimental process of Pb^{2+} ions on adsorbents was shown in Figure 1. Lead ion solutions with different concentrations of 200, 400 and 800 mg/L were prepared by adding $Pb(NO_3)_2$ into deionized water. The pH values of the solutions were adjusted at 2.5, 4.0, 5.5 and 7.0 by a HNO_3 solution (0.1 M) or a NaOH solution (0.1 M) at 25°C. HCPMs (0.5 g) and CPMs (0.5 g) were cut into cylinder (Φ 12 mm), respectively. After the adsorbents were put into sample tube, the Pb^{2+} solutions flowed down through the tube at a flow rate of 0.8 ml/min. In addition, filter paper was put into sample tube. The HAP powders (0.5 g) were added on the filter paper, and then the Pb^{2+} solutions flowed down through the tube at a flow rate of 0.8 ml/min. At the given time intervals, the concentrations of Pb^{2+} ions in the solution were determined by inductively coupled plasma/optical emission spectrometry (ICP/OES, Perkin Elmer, OPTIMA 3300 DV). All experimental data were the average of duplicate determinations, and the relative errors were about 1.0%. The cumulative adsorption efficiency (A_t) and cumulative adsorption amount (q_t) were calculated according to the following equations:

$$A_t = \frac{c_o - c_t}{c_o} \times 100\% \quad (1)$$

$$q_t = \frac{(c_o - c_t)V}{m} \quad (2)$$

where c_o (mg/L) was the initial concentration of Pb^{2+} ions, c_t was the concentration at a given time, m is the weight of CPMs or HCPMs, and V is the volume of outflow solutions.

2.4 Characterization

The morphologies and microstructures of samples were investigated by scanning electron microscopy (SEM, Hitachi S-4800, CamScan) with energy-dispersive spectrometry (EDS). The crystalline phases of samples were examined with X-ray powder diffraction (XRD, D/max-II B, Japan) using CuKα radiation (λ=1.541874Å) within the scanning range of $2\vartheta=10^o$ to 80^o at a scanning rate of 4^o min^{-1} and a step size of 0.02^o. Fourier transform infrared spectra (FTIR, Nicolet 5DX) were collected to analyze functional groups at room temperature by using the KBr pellet technique, working in the range of wavenumbers 4000-400 cm^{-1} at a resolution of 2 cm^{-1}. N_2 adsorption-desorption isotherms were measured with an automatic surface area and porosity analyzer (AUTOSORB-1-C, Quantachrome) at -203.85°C. The pore size distributions were derived from desorption branches of isotherms by using the Barrett-Joyner-Halanda (BJH) method. Zeta potential of the samples was determined by using ZetasizerNano-ZS90 (Malvern Instruments). The mechanical property of HCPMs and CPMs were characterized by a universal material testing machine (WDW-20C, Shanghai Hualong Test Instruments Corporation, China) with a specimen size of 10 mm height and 12 mm diameter. The porosity (π) of CPMs and HCPMs were measured by liquid displacement method.[40] The samples were immersed into absolute ethanol under vacuum conditions until they were saturated by absorbing ethanol. The porosity of the porous materials was calculated according to the formula:

$$\pi = \frac{W_1 - W_o}{\rho V_o} \times 100\% \quad (3)$$

where W_o were the weight of dry porous materials, W_1 were the weight of porous materials saturated by absorbing ethanol, V_o was the total volume of porous materials, and ρ was the density of ethanol.

3. Results and discussion

3.1 Characterization of HCPMs before and after adsorbing Pb2+ ions

HCPMs have great potentials for the removal of heavy metal ions. The preparation process of the HCPMs includes the following steps: (i) freeze-drying fabrication of BCPMs; and (ii) conversion of HCPMs from BCPMs after alkaline solution treatment, as shown in Scheme 1. In the first stage, the BCPMs were prepared after the mixtures including CS, Ca^{2+} ions and PO_4^{3-} ions were treated by freeze-drying method (Scheme 1a). The mixtures including chitosan, Ca^{2+} ions and PO_4^{3-} ions were prepared by the addition of $Ca(NO_3)_2{\cdot}4H_2O$ and $NaH_2PO_4{\cdot}2H_2O$ into chitosan/acetic acid solutions. Since $Ca(NO_3)_2$ and NaH_2PO_4 can be dissolved in acetic acid solutions, no calcium phosphate phases exist in the mixtures solutions. After freeze-drying treatment, the BCPMs were formed due to the volatilization of acetic acid. The XRD pattern in Figure S1 indicates that the main inorganic phase of these porous materials is DCPD ($CaHPO_4{\cdot}2H_2O$). The morphologies of the BCPMs are shown in SEM images, and CPMs serve as the control group (Figure 2). The low-resolution SEM images of cross sections and longitudinal sections indicate that both samples possess 3D interconnected macroporous structure (Figure 2a, b, d and e). The macropores are produced by using ice crystals as sacrificial templates during the freeze-drying process. The thin films in the BCPMs exhibit rough surfaces originated from DCPD particles (Figure 2g and j), while those in the CPMs have smooth and dense surfaces due to the high molecular weight and polymeric nature (Figure 2h and k).

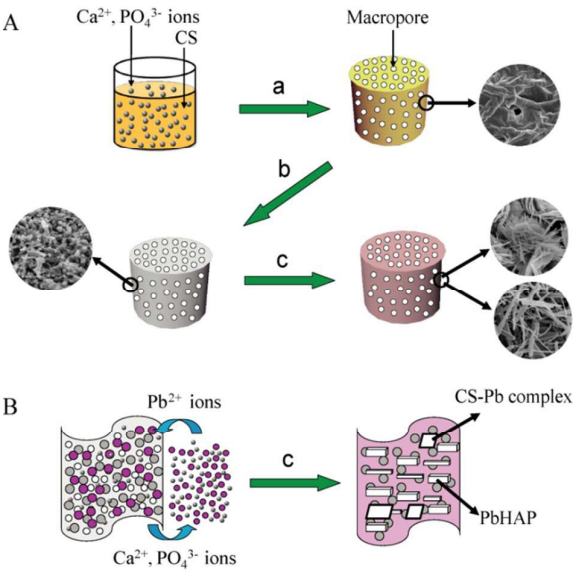

Scheme 1. (A) Illustration of the preparation process of HCPMs and their adsorption process for Pb^{2+} in aqueous solutions under flow conditions: (a) fabrication of BCPMs from CS solutions including Ca^{2+} ions and PO_4^{3-} ions by freeze-drying method; (b) conversion of HCPMs from BCPMs after NaOH solution treatment; (c) adsorption of Pb^{2+} ions on HCPMs under flow conditions to form PbHAP rods and CS-Pb complex. (B) Illustration of adsorption mechanism of HCPMs for Pb^{2+} ions in aqueous solutions.

In the second stage, HCPMs were converted from the BCPMs by alkaline solution treatment (Scheme 1b). Because the logarithmic solubility product of DCPD (pK_{sp}=6.622) is lower than that of HAP (pK_{sp}=58.6), HAP is more stable than DCPD in solution. After soaking in a NaOH solution at 37°C for 3 days, the Ca^{2+} and PO_4^{3-} ions are released from DCPD in the BCPMs, and react with OH^- ions to form *in situ* HAP particles on the thin films (Figure 2i and l). The nano-HAP rods with a length of ~500 nm and a diameter of ~20 nm are uniformly distributed on the thin films of the HCPMs. The low-resolution SEM images indicate that the HCPMs have a similar porous structure to the BCPMs (Figure 2c and f). The 3D connected macropores improve remarkably porosity, and thus give rise to increasing adsorption property of heavy metal ions.[41] The total

porosity of porous materials is estimated by using liquid displacement method. The porosities of the HCPMs and CPMs are 93.0% and 94.4%, respectively. The pore size distribution curves are determined according to the SEM image of the HCPMs and CPMs (Figure S2). The pore size of the HCPMs is mainly distributed around 150~240 μm, while that of the CPMs is mainly distributed around 60~180 μm. The bigger pore size of the HCPMs than the CPMs is attributed to the presence of inorganic materials. The pore size of the HCPMS is similar to the BCPMs, because the former is converted from the latter. The Ca^{2+} ions in DCPD can bond to CS via complexing action, which decreases pore shrinkage during the vaporization process of ice-crystal after freezing. The mesoporous structures of the HCPMs and CPMs are characterized by N_2 adsorption-desorption isotherms and corresponding BJH pore size distribution curves, as shown in Figure S3. The CPMs exhibit the type III isotherm without hysteresis loop, suggesting that they do not have mesoporous structure (Figure S3a). Interestingly, the curves of the HCPMs are identified as type IV isotherm with type H3 hysteresis loops (Figure S3b). The type H3 loop, which does not exhibit any limiting adsorption at high P/P_o, is attributed to the aggregation of nano-HAP particles giving rise to slit-shaped pores, as revealed by the SEM image in Figure 2l. The corresponding BJH pore size distribution curve indicates that the pore size was distributed around 3.70-6.77 nm (Figure S3b, inset). The mesopores in the HCPMs make them have larger BET surface area and pore volume than the CPMs. The BET surface area and pore volume of the HCPMs are 37.10 m^2/g and 0.073 cm^3/g, respectively, while those of CPMs are only 13.11 m^2/g and 0.018 cm^3/g. The large specific surface area and porous structure are important factors for achieving a high heavy metal adsorption amount.

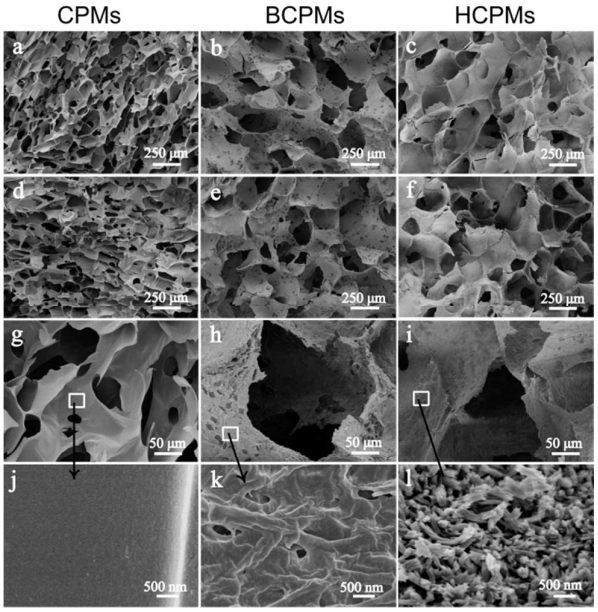

Figure 2. SEM images of CPMs, BCPMs and HCPMs: (a-c) cross section view; (d-f) longitudinal section view; (g-l) high-resolution images.

The XRD patterns and FTIR spectra are used to investigate the structures of the HCPMs, and the CPMs and HAP powders serve as control samples. The XRD pattern indicates that the characteristic peaks due to CS and HAP are observed in the HCPMs (Figure 3c, left). As a semi-crystalline material, CS exhibits the characteristic peaks at 2ϑ=20.30° and 28.11° (Figure 3a). The characteristic peaks due to HAP locate at 2ϑ=26.03°, 29.04°, 31.73°, 32.81°, 33.97°, 39.74°, 46.98°, 49.97° and 64.28° (JCPDS card no. 09-0432, Figure 3b). The HAP crystals in the HCPMs belong to $P6_3/m$ space group with crystal parameters $a = b = 0.942$ nm, $c = 0.687$ nm, $\alpha = \beta = 90°$ and $\gamma = 120°$. According to the results of XRD pattern, the theoretical compositions of HAP and CS in the HCPMs are 33.4 wt% and 66.6 wt%, respectively. In addition, the functional groups in the CPMs, HAP powders and HCPMs are detected by FTIR spectra (Figure 3, right). For the CPMs (Figure 3a, right), N-H stretching vibration occurs in the 3420-3220 cm^{-1} region overlapping the -OH stretch from the carbohydrate ring.[42] The bands at 2920 and 2879 cm^{-1} are corresponded to the C-H stretching vibration in -CH and $-CH_2$ groups in CS.[43,44] The bands at 1655 cm^{-1} and 1604 cm^{-1} are assigned to the C=O bond stretching of amide I and N-H deformations of amide II, respectively.[45,46] The bands at 1400 cm^{-1}, 1318 cm^{-1} and 1261 cm^{-1} are corresponded to C-H bending vibration, CH_3 symmetric stretching vibration and C-O-H stretching vibration, respectively.[47] The bands at 1154 cm^{-1} and 1036 cm^{-1} are assigned to C-O-C stretching vibration modes.[48] For the HAP powders (Figure 3b, right), the intense absorption peak at 1033 cm^{-1} is ascribed to the stretching vibration (v_3) of the phosphate (PO_4^{3-}) groups, and the peaks at 563 cm^{-1} and 604 cm^{-1} are ascribed to the bending vibration (v_4) of the phosphate (PO_4^{3-}) groups in HAP phase.[49] The absorption band due to HPO_4^{2-} at around 1103 cm^{-1} indicates that the samples are calcium-deficient HAP.[50] The hydroxyl absorption band due to HAP locates at 638 cm^{-1}.[51] For the HCPMs, the characteristic bands of both CS and HAP are detected in the FTIR spectrum (Figure 3c, right). The C=O bond of amide I at 1655 cm^{-1} shifts to a lower band 1637 cm^{-1}, which suggests that the interaction between $-NH_2$ groups in CS and -OH groups in HAP as well as chelating between $-NH_3^+$ and Ca^{2+}. Moreover, other characteristic peaks due to CS are detected in Figure 3c (right), although some peaks are overlapped by those of HAP.

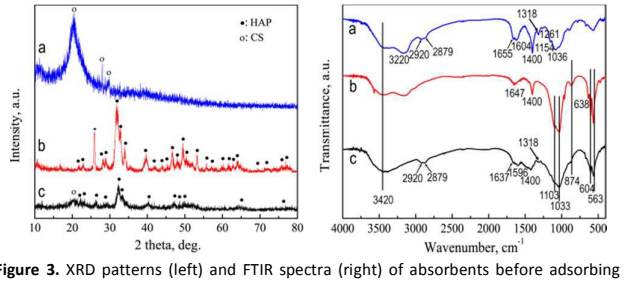

Figure 3. XRD patterns (left) and FTIR spectra (right) of absorbents before adsorbing Pb^{2+} ions: (a) CPMs; (b) HAP powders; (c) HCPMs.

Mechanical property is an important parameter for porous materials. Figure S4 shows the relation curves of the compression strength and displacement for the HCPMs and

CPMs. The CPMs are soft ductile materials, so they exhibit poor compression strength (Figure S4a). When compressed by an external force, the CPMs undergo only compression deformation, without a brittle facture process. Interestingly, the HCPMs have the good compression strength of 0.98±0.05 MPa (Figure S4b), which may be attributed to their hybrid composite materials. Pure HAP is a brittle material, while CS is a soft ductile material. The HCPMs combine the strong hardness of HA crystals with the good tensile property of CS. In addition, both the CPMs and HCPMs possess macropores with the pore sizes of approximately 60~180 μm and 150~240 μm, respectively (Figures 2 and S2). The high porosities of the HCPMs and CPMs may decrease their mechanistic properties.

At the final stage, Pb^{2+} adsorption experimental was carried out by the flow of a lead solution through absorbents (Scheme 1c). The HCPMs possess good adsorption properties because the nano-HAP is converted to PbHAP via a dissolution-precipitation reaction. Moreover, the CS in the porous materials chemically absorbs Pb^{2+} ions by forming CS-Pb complex. The above conclusions are confirmed by the changes of the HCPMs in phases, functional groups and morphologies between before and after adsorbing Pb^{2+} ions. The phase structures of the HCPMs after adsorbing Pb^{2+} ions are characterized by XRD patterns by using the CPMs and HAP powders as control samples (Figure 4, left). After adsorbing Pb^{2+} ions for 168 h, the characteristic peaks due to CS-Pb complex are detected in the CPMs (Figure 4a, left). During the chemical adsorption process of Pb^{2+} ions, the CS in the porous materials bonds to Pb^{2+} ions and forms CS-Pb complex (Figure 4a, left), as confirmed by the phase changes of the CPMs before and after adsorbing Pb^{2+} ions (Figure 3a, left). For the HAP powders after adsorbing Pb^{2+} ions, the characteristic peaks of PbHAP are detected, while the peak strength of HAP decreases (Figure 4b, left). The above result suggests that most of HAP is converted to lead hydroxyapatite (PbHAP, $Pb_{10}(PO_4)_6(OH)_2$, JCPDS card no. 08-0259) after HAP powders adsorb Pb^{2+} ions. Interestingly, the characteristic peaks due to both the CS-Pb complex and PbHAP are observed in the HCPMs after adsorbing Pb^{2+} ions (Figure 4c, left). The PbHAP crystals in the HCPMs belong to $P6_3/m$ space group with crystal parameters a = b = 0.986 nm, c = 0.745 nm, α= β= 90° and γ = 120°.

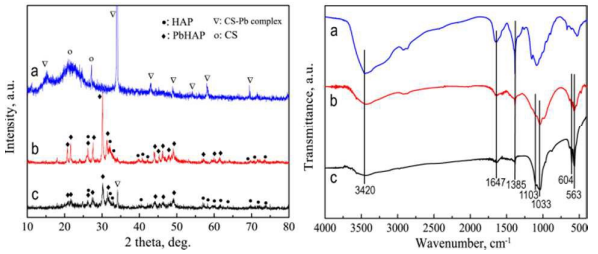

Figure 4. XRD patterns (left) and FTIR spectra (right) of absorbents after adsorbing Pb^{2+} ions: (a) CPMs; (b) HAP powders; (c) HCPMs.

The functional groups of the CPMs, HAP powders and HCPMS after adsorbing Pb^{2+} ions are demonstrated by FTIR spectra (Figure 4, right). For the CPMs after adsorbing Pb^{2+} ions, the band at 1655 cm^{-1} disappears and the band at 1400 cm^{-1} shifts to lower band at 1385 cm^{-1}, suggesting that the Pb^{2+} ions predominately are associated with -NH_2 group. For both the HAP powders and HCPMs, the characteristic bands of PO_4^{3-} and OH groups do not change after adsorbing Pb^{2+} ions (Figure 4b and c). In addition, the weak changes from 1300~1660 cm^{-1} are detected, indicating the chelating of -NH_2 group with Pb^{2+} ions (Figure 4c, right). The results of both the XRD patterns and FTIR spectra suggest that the good lead adsorption property of the HCPMs is ascribed to the formation of the CS-Pb complex and PbHAP.

The low-resolution SEM images indicate that the macroporous structure of the HCPMs after adsorbing Pb^{2+} ions is similar to that before adsorbing Pb^{2+} ions (Figures 2c, 2f and 5a), suggesting that the lead solutions with pH=5.0 are scarcely damaged 3D macropores structure. Notably, obviously morphology differences of the HCPMs are observed between before and after adsorbing Pb^{2+} ions under the high-resolution SEM images (Figures 2l, 5c and 5d). The nano-HAP particles in the HCPMs exhibit nanorod-like shape with a length of only ~500 nm and a diameter of only ~20 nm. After adsorbing Pb^{2+} ions on the HCPMs, lots of PbHAP rods with a length of 1~3 μm and a diameter of 50~200 nm are detected (Figure 5c). The great changes of the HCPMs in phases and morphologies between before and after adsorbing Pb^{2+} ions suggest that the conversion mechanism of nano-HAP into PbHAP is a dissolution-precipitation reaction rather than an ion-exchange reaction.

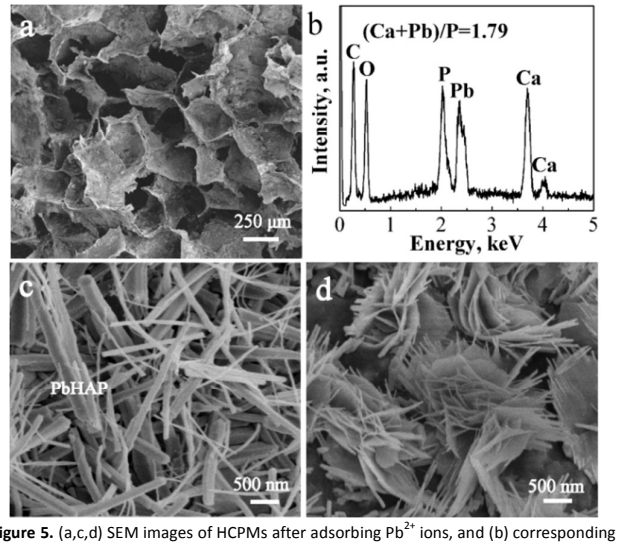

Figure 5. (a,c,d) SEM images of HCPMs after adsorbing Pb^{2+} ions, and (b) corresponding EDS spectrum.

In addition, many nanoplates surrounded by nanorods are detected in the HCPMs after adsorbing Pb^{2+} ions (Figure 5d). These nanoplates could be attributed to CS-Pb complex (Figure 4c, left). In order to confirm the above conclusions, the morphology and phase of the CPMs after adsorbing Pb^{2+} ions are investigated by XRD pattern and SEM image, as shown in Figures 4a and 6. The films in the CPMs exhibit smooth surfaces (Figure 2a-c), while many plate-like particles are

detected on the films after adsorbing Pb^{2+} ions (Figure 6). These plates are CS-Pb complex, as confirmed by the XRD pattern (Figure 4a, left), FTIR spectrum (Figure 4a, right) and Pb element distribution image (Figure 6d). The characteristic peaks of both CS and CS-Pb complex are detected in the CPMs after adsorbing Pb^{2+} ions (Figure 3a, left). Moreover, the Pb elements are mainly distributed around the above CS-Pb particles (Figure 6b). For the HCPMs, the CS in the adsorbents can react with Pb^{2+} ions to form plate-like CS-Pb complex (Figures 4c and 5d). Since the percentages of CS in the HCPMs are lower than the pure CPMs, the size of the CS-Pb complex in the former is smaller than that in the latter. Interestingly, the CS-Pb complex plates are surrounded with many nanorods. These nanorods may be attributed to PbHAP (Figure 5d), because the CS-Pb complex serve as active sites to promote the deposition of PbHAP nanorods.

Figure 5b shows the EDS spectrum of HCPMs after adsorbing Pb^{2+} ions. The C element is derived from CS, the Ca element is derived from HAP, the P element is derived from PbHAP and HAP, the O element is derived from CS, HAP and PbHAP, and the Pb element is derived from PbHAP, CS-Pb complex. Generally, the Ca/P ratio of stoichiometric HAP and the Pb/P ratio of stoichiometric PbHAP are 1.67. However, the EDS spectrum clearly shows the (Ca+Pb)/P ratio of the HCPMs after adsorbing Pb^{2+} ions is 1.79, which is higher than stoichiometric apatite. The reason is attributed to physical adsorption of Pb^{2+} ions and presence of CS-Pb complex in the HCPMs after adsorbing Pb^{2+} ions.

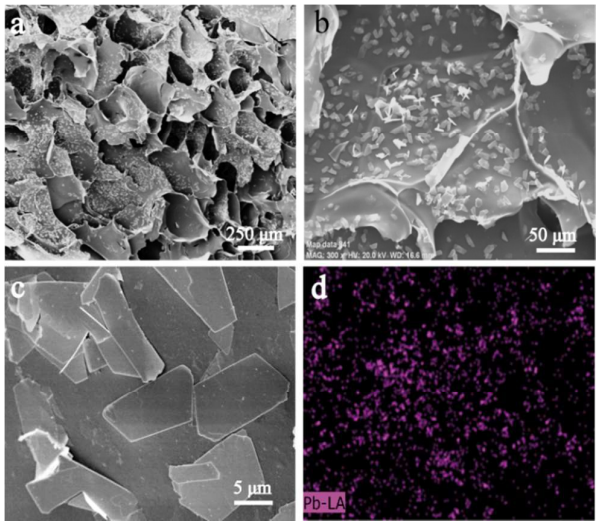

Figure 6. (a,b,c) SEM images of CPMs after adsorbing Pb^{2+} ions, (d) Pb element distribution image corresponding to (b).

3.2 Adsorption performance of Pb^{2+} ions on HCPMs

HCPMs can chemically adsorb Pb^{2+} ions in lead solutions by forming PbHAP and CS-Pb complex (Figures 4-5). To evaluate the adsorption ability of the HCPMs for Pb^{2+} ions, the absorption experiment were carried out by the flow of lead aqueous solutions through the adsorbents at 25°C. The flow rate was controlled at 0.8 ml/min, and the concentration of the Pb aqueous solution was 400 mg/L. According to the acidic nature of the industrial wastewaters, the pH values are controlled at 2.5~7.0. The SEM images, XRD patterns and FTIR spectra suggest that the chemical compositions of the HCPMs include CS and HAP powders (Figures 2 and 3), so the CPMs and HAP powders serve as control samples in the present work (Figure 7).

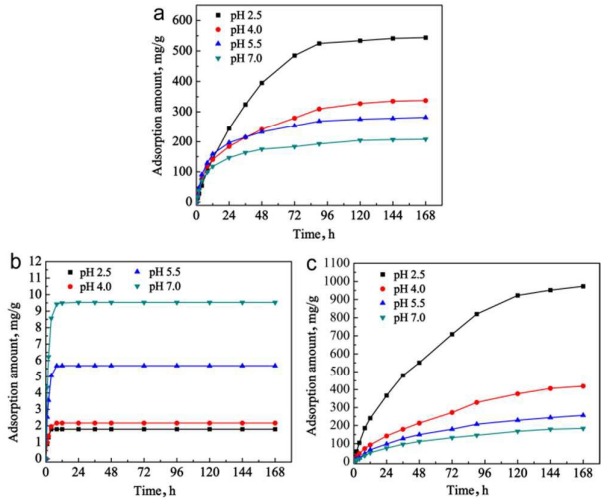

Figure 7. Cumulative adsorption amounts of Pb^{2+} ions on samples at different time under the lead solutions with a concentration of 400 mg/L: (a) HCPMs; (b) CPMs; (c) HAP powders.

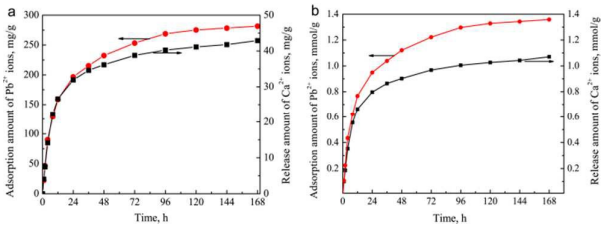

Figure 8. The lead solution with the pH value of 5.5 and concentration of 400 mg/L flow throughout HCPMs: (a) cumulative adsorption amounts of Pb^{2+} ions on HCPMs and corresponding release amounts of Ca^{2+} ions at different time; (b) comparison of molar adsorption amounts of Pb^{2+} ions on HCPMs and corresponding molar release amounts of Ca^{2+} ions at different time.

The adsorption amounts of Pb^{2+} ions on the CPMs increase during the first 8 h, but then reach the adsorption equilibrium upon increasing further the time (Figure 7b). Under the different lead solutions with pH values of 2.5, 4.0, 5.5 and 7.0, the experimental equilibrium adsorption amounts on the CPMs are 1.8, 2.2, 5.7 and 9.5 mg/g, respectively. Notably, the adsorption amounts of Pb^{2+} ions on the CPMs gradually reduce with decreasing the pH values of the lead solutions. The reason may be attributed to the fact that the low pH values accelerate the protontion of CS, and thus weaken the adsorption of Pb^{2+} ions on the CPMs. Figure 7c indicates that the adsorption amounts of Pb^{2+} ions on the HAP powders increase during the first 120 h, but then reach the adsorption equilibrium upon increasing further the time. The pH values of lead solutions have great effects on the adsorption property of the HAP

powders, too. With the decrease of pH values, the maximum adsorption amounts of Pb^{2+} ions increase at different time (Figure 7c). Under the different lead solutions with pH values of 2.5, 4.0, 5.5 and 7.0, the experimental equilibrium adsorption amounts on the HAP powders are 973.0, 419.0, 256.6 and 183.7 mg/g, respectively. For the HCPMs, the adsorption amounts of Pb^{2+} ions increase during the first 96 h, but then reach the adsorption equilibrium. With the decrease of pH values, the maximum adsorption amounts of Pb^{2+} ions increase (Figure 7a). Under the different lead solutions with pH values of 2.5, 4.0, 5.5 and 7.0, the experimental equilibrium adsorption amounts on the HCPMs are 543.9, 337.7, 281.7 and 208.0 mg/g, respectively.

The above results reveal that the adsorption property of adsorbents is related to chemical compositions, and the order is as follows: HAP powders > HCPMs > CPMs. Although the cumulative adsorption amounts of Pb^{2+} ions on three samples increase with prolonging adsorption time, the adsorption rates decrease gradually (Figures 7 and S5). Unfortunately, the CPMs have bad adsorption property for Pb^{2+} ions, and adsorption rate (cumulative adsorption amount/adsorption time) reduces to 0 after 12 h (Figure S5b). In contrast, the HAP powders and HCPMs exhibit great adsorption rate for Pb^{2+} ions, especially at a pH value of 2.5 (Figure S5a and c). The HAP powders possess the greatest adsorption amounts among three samples, but they do not have a great industrial application potential because of their difficult separation from wastewaters. Notably, the Pb^{2+} ions adsorption curves on the HCPMs as a function of adsorption time and pH value are similar to the HAP powders rather than the CPMs (Figure 7a and b), suggesting that the adsorption performance of the HCPMs is mainly determined by the nano-HAP in the porous materials. The cumulative adsorption amounts of Pb^{2+} ions on the HCPMs have similar trends to the cumulative release amounts of Ca^{2+} ions (Figure 8a). The molar amount of Ca^{2+} ions released from the HCPMs is close to that of adsorbed Pb^{2+} ions, and the former is lower than the latter at different time, especially after 12 h (Figure 8b). Approximately 78.8% Pb^{2+} ions are adsorbed on the HCPMs by forming PbHAP, which is estimate according to the ratio (molar amount of the Ca^{2+} ions released from the HCPMs/molar amount of the adsorbed Pb^{2+} ions) (Figure 8b). The above results suggest that the adsorption amounts of Pb^{2+} ions on the HCPMs are mainly attributed to the conversion of nano-HAP to PbHAP. The excess molar amount of the adsorbed Pb^{2+} ions over the released Ca^{2+} ions are mainly ascribed to the following reasons including: (i) chemical adsorption of Pb^{2+} ions by forming CS-Pb complex; and (ii) physical adsorption of Pb^{2+} ions on the porous materials via electrostatic interaction. Approximately 2.0% Pb^{2+} ions is adsorbed on the HCPMs by forming CS-Pb complex, which is estimate according to the ratio (Pb^{2+} adsorption amount on CPMs/Pb^{2+} adsorption amount on HCPMs) at adsorption equilibrium condition (Figure 7). Under the lead solutions with the pH value of 5.5 and concentration of 400 mg/L, approximately 19.2% Pb^{2+} ions are adsorbed on the HCPMs by physical adsorption. The physical adsorption property of adsorbents is determined by their porous structure, surface area and zeta potential. The HCPMs have maroporous structure with the pore size around 150~240 μm and mesoporous structure with the pore size around 3.70-6.77 nm (Figures 2c, 2f and S3b). The macropores and mesopores not only provide transfer channels for adsorbing metal ions, but also increase the specific surface areas for achieving a high adsorption amount of Pb^{2+} ions. The zeta potential of the HCPMs decreases with the increase of pH value (Figure S6), suggesting that their physical adsorption for metal ions might increase, too.

3.3 Adsorption mechanism of Pb^{2+} ions on HCPMs

Recently, many adsorbents including HAP/polyacrylamide, HAP, HAP/polyurethane, HAP/Fe_3O_4 microspheres, activated carbon, CS, CS–palygorskite composites, polyacrylamide-grafted iron(III) oxide and 2,4-dinitrophenylhydrazin modified Al_2O_3 were developed to remove heavy metal ions. Table 1 shows the maximum sorption capacity of different adsorbents for the removal of Pb^{2+} ions under different experimental conditions. It is seem that the maximum Pb^{2+} sorption capacity of the HCPMs is greater than most of other adsorbents (Figure 7a and Table 1). Moreover, the HCPMs have greater advantage than adsorbent powders in the effective separation of adsorbents from wastewater under flow conditions.

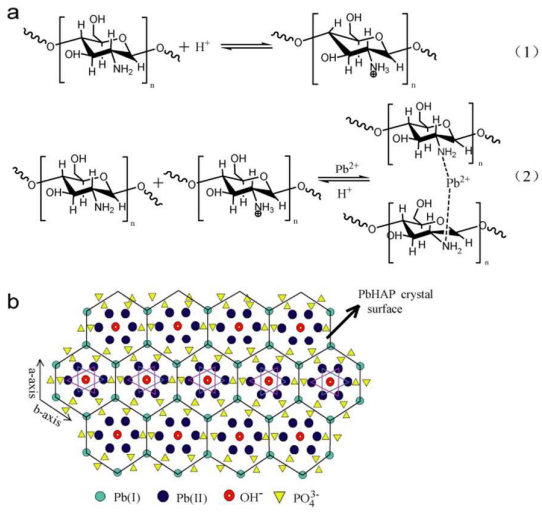

Figure 9. (a) Equations on intermolecular complexes of CS with Pb^{2+} ions in acid solutions under flow conditions; (b) schematic diagram of PbHAP crystal structure viewed along *a*(*b*)-axis.

The HCPMs possess excellent adsorption property for Pb^{2+} ions (Figure 7a), which is ascribed to their chemical compositions including CS and HAP. The adsorption mechanism of Pb^{2+} ions on the HCPMs are illustrated in Scheme 1. As we know, CS consists of β-(1,4)-2-actamido-2-β-D-glucose and β-(1,4)-2-amido-2-β-D-glucose units. CS adsorbs heavy metal ions via its binding sites such as amino (-NH_2) and secondary alcohol (-OH) functional groups. The nitrogen in amino group and the oxygen in hydroxyl group have an available pair of electrons that form coordinated covalent bonds with metal ions (M^{2+}). The oxygen atom in hydroxyl group has a stronger attraction to its electron lone pairs than

the nitrogen atom in amino group, so the amino group is more likely to donate the lone pairs to metal ions.[43] Under an acidic condition, the formation process of CS-Pb complex can be expressed by the chemical equations in Figure 9a. Xua et al. have reported that the protonated-NH_2 in acid solutions has big influence on the adsorption capacity of Cu^{2+} ions on porous CS monolithis.[68] The initial pH value of metal solutions has great effects on the degree of protonation, too. For example, if the pH value is controlled at 4.0, 99.0% of amino groups in CS are protonated.[69] At the pH value of 5.5, part of -NH_2 groups are protonated. The above conclusion can be confirmed by the experimental result that the zeta potential of the CPMs decreases with increasing pH value (Figure S6). Under an acidic condition, the ion exchange reaction takes place by the substitution of H^+ ions by Pb^{2+} ions because the electrical attraction of Pb^{2+} ions is stronger than H^+ in binding with -NH_2 (Figure 9a). At the same time, the –NH_2 as basic functional groups can directly bond to Pb^{2+} ions to form CS-Pb complex. The as-formed plate-like CS-Pb particles are confirmed by XRD patterns (Figure 4a) and SEM images (Figure 6). Although CS can chemically adsorb Pb^{2+} ions under acidic or basic solution, the pH value has a great effect on the adsorption amount. Figure 7b indicates that the experimental equilibrium adsorption amounts of Pb^{2+} ions on the CPMs increase from 1.8 mg/g to 9.5 mg/g as the pH values of lead solutions increase from 1.5 to 7.0. One of important reasons may be attributed to the different stabilities of CPMs under different pH values. Under strong acid solutions, Pb^{2+} ions may be desorbed from the CPMs because of the dissolution of CS. Therefore, the CPMs possess the greater adsorption amount for Pb^{2+} ions under the higher pH value.

Table 1. Comparison of maximum adsorption amounts of different adsorbents for Pb^{2+} ions

Adsorbents	Type	C_o (mg/L)	pH	q_{max}(mg/g)	Ref.
HAP	powder	1000-8000	3.0-5.0	330.0-450.0	52
Nano-HPA	powder	414	5.5	242.4	53
HAP/polyacrylamide composite hydrogels	hydrogel	50-300	2-5	123.0-209.0	54
HAP/ polyurethane composite foams	porous materials	44-184	5.0	150.0	55
HAP/Fe_3O_4 microspheres	powder	600	3.0	440	56
NanoHAP-alginate composite adsorbents	powder	900	6.2-7.1	270.3	57
CS	bead	50	5.5	79.2	58
CS–palygorskite composites	bead	400	4.0	147.1-201.5	59
CS/magnetite composite	bead	50-80	6.0	63.3	60
CS-tripolyphosphate beads	bead	20-300	3-6	57.3	61
polyving alcohol/polyacrylic acid gel	gel	350	4.0	194.99	62
Modified quebracho tannin resin	resin	150	5.0	86.2	63
Activated carbon	powder	20-200	6.0	21.8	64
2,4-dinitrophenylhydrazin modified Al_2O_3	powder	50	5.0	100.0	65
polyacrylamide-grafted iron(III) oxide	hydrogel	100-400	6.0	211.4	66
Soy Protein Hollow Microspheres	powder	200	5.5	235.6	3
Carboxylated cellulose nanofibrils-filled magnetic chitosan hydrogel beads	hydrogel	300	4.0-4.5	171.0	67

Besides CS, the nano-HAP particles in HCPMs have great contribution to absorb Pb^{2+} ions in a lead solution. Previous reports have demonstrated that the Ca^{2+} ions in HAP crystal lattices can be substituted by other metallic cations (Cu^{2+}, Cr^{3+}, Ni^{2+}, Pb^{2+}, Hg^{2+}, Fe^{3+}, et al.) by an ion exchange reaction.[33-36] The HCPMs possess many thin films, which aggregate to form 3D macropores with a pore size of 150~240 μm (Figures 2c and 2f), and the nano-HAP rods with a length of ~500 nm and a diameter of ~20 nm are dispersed uniformly on the films (Figure 2l). After the Pb^{2+} solution is flowed through the HCPMs by using the macropores as channels, the PbHAP rods with a length of 1~3 μm and a diameter of 50~200 nm are produced (Figures 4 and 5). The remarkable changes in the morphologies and phases of the HCPMs between before and after absorbing Pb^{2+} ions indicate that the conversion mechanism of nano-HAP particles into PbHAP is not an ion exchange reaction but a dissolution-precipitation reaction. After lead solutions flow through the HCPMs, the dissolution reaction of HAP occurs:

$$Ca_{10}(PO_4)_6(OH)_2 \rightarrow 10Ca^{2+} + 6PO_4^{3-} + 2OH^- \quad (4)$$

The logarithmic solubility product constant of PbHAP (pK_{sp}=125.6) at 25°C is lower than that of HAP (pK_{sp} =76.3),[70] so HAP is easily converted into PbHAP. The released of PO_4^{3-} ions and OH^- ions increases the local ions concentration around the nano-HAP crystals in HCPMs. As the ionic activity product exceeds the thermodynamic solubility product of PbHAP crystals, they *in situ* deposit on the surfaces of the HCPMs by

using the HAP and CS as active sites (Figure 5). The formation mechanism of PbHAP is expressed by the following equation:

$$10\,Pb^{2+} + 6\,PO_4^{3-} + 2\,OH^- \rightarrow Pb_{10}(PO_4)_6(OH)_2 \quad (5)$$

Since PbHAP has the same hexagonal symmetry ($P6_{3/m}$) as HAP, they exhibit rod-like shapes (Figure 5c). For both the HCPMs and HAP powders, HAP particles are converted to PbHAP nanorods by a dissolution-precipitation reaction (Eq. 4 and 5). As we know, the HAP particles can be dissolved in acid solutions, and their dissolution rate increases with decreasing the pH value. The released PO_4^{3-} ions can promote the chemical adsorption of the HCPMs and HAP powders for Pb^{2+} ions by the formation of PbHAP. Therefore, the Pb adsorption capacities of both the HAP powders and HCPMs increase with the decrease of pH values (Figure 7a and c).

The HCPMs as ideal adsorbents for removal of Pb^{2+} ions must have good adsorption property and stability. Figure 7a indicates that the Pb adsorption amounts of the HCPMS arrive at 208.0~543.9 mg/g under the lead solutions with pH=2.5~7.0. Although the adsorption property of the HCPMs is less than the pure HAP powders, the former possesses greater industrial application potential than the latter because of their easy separation from wastewaters. Moreover, the microstructure of the HCPMs is stable even after adsorbing Pb^{2+} ions for 168 h in lead solutions with pH values of 2.5-7.0 (Figure S7).

3.4 Adsorption kinetics of Pb^{2+} ions on HCPMs

An ideal adsorbent for the removal of heavy metal ions should not only have a large adsorption capacity but also possess fast adsorption rate.[71] Adsorption kinetics provides the necessary information on reaction pathway and adsorption dynamics. The sorption behaviors of Pb^{2+} ions on HCPMs are verified using Lagargren's pseudo-first-order and chemisorption's pseudo-second-order kinetic models.[72-74] The models are used to analyze the controlling mechanism of adsorption process.

The simple form of pseudo-first-order equation was given as:

$$\log(q_e - q_t) = \log q_{e,cal} - \frac{k_1}{2.303}t \quad (6)$$

where q_t (mg·g^{-1}) is the adsorption amount of Pb^{2+} ions on the CS and HCPMs at any time t (h); q_e (mg·g^{-1}) is experimental equilibrium adsorption amount; $q_{e,cal}$ (mg·g^{-1}) is theoretical equilibrium adsorption amount; and k_1 (h^{-1}) is pseudo-first-order rate constant. The plot of log(q_e-q_t) versus t for pseudo-first-order kinetics shows a linear relationship. The adsorption rate constant (k_1) and theoretical equilibrium adsorption amount ($q_{e,cal}$) are calculated according to the slopes and intercepts in the curves of log(q_e-q_t) versus t.

The pseudo-second-order kinetic model is shown as follows:

$$\frac{t}{q_t} = \frac{1}{k_2 q_{e,cal}^{\ 2}} + \frac{t}{q_{e,cal}} \quad (7)$$

where k_2 (g·mg^{-1}·h^{-1}) is adsorption rate constant for pseudo-second-order kinetic model, and q_t (mg·g^{-1}) is adsorption amount of Pb^{2+} ions on adsorbents at any time t (h). The constants $q_{e,cal}$ and k_2 values are calculated from the slopes and intercepts in the curves of t/q_t versus t. The initial adsorption rate of Pb^{2+} ions is expressed as $h_i = k_2 q_{e,cal}^{\ 2}$ (g·mg^{-1}·h^{-1}), which is calculated according to pseudo-second-order kinetic model.

Table 2. Pseudo-first-order kinetic constants and pseudo-second-order kinetic constants for the HCPMs , CPMs and HAP powders.

Adsorbents	pH	Experimental values	Pseudo-first-order kinetics model			Pseudo-second-order kinetics model			
		q_e (mg/g)	$q_{e,cal}$ (mg/g)	k_1 (h^{-1})	R^2	$q_{e,cal}$ (mg/g)	k_2 (g·mg^{-1}·h^{-1})	R^2	h_i (mg·g^{-1}·h^{-1})
HCPMs	2.5	543.9	625.6	0.0359	0.9860	729.9	2.92×10^{-5}	0.9881	15.6
	4.0	337.7	332.3	0.0299	0.9720	374.5	1.36×10^{-4}	0.9938	19.1
	5.5	281.7	217.1	0.0297	0.9873	303.0	2.77×10^{-4}	0.9993	25.5
	7.0	208.0	163.3	0.0309	0.9769	220.8	4.06×10^{-4}	0.9991	19.8
CPMs	2.5	1.8	1.8	0.645	0.9948	1.8	2.08	0.9999	6.7
	4.0	2.2	3.4	0.879	0.9560	2.2	1.07	0.9999	5.1
	5.5	5.7	9.1	0.877	0.9496	5.7	0.39	0.9999	12.7
	7.0	9.5	8.2	0.495	0.9832	9.6	0.24	0.9999	22.1
HAP powders	2.5	973.0	1066.0	0.0244	0.9662	1250.0	1.61×10^{-5}	0.9851	25. 2
	4.0	419.0	451.8	0.0207	0.9474	531.9	3.54×10^{-5}	0.9536	10.0
	5.5	256.6	258.0	0.0193	0.9889	323.6	6.23×10^{-5}	0.9891	6.5
	7.0	183.7	193.9	0.0228	0.9521	232.6	9.09×10^{-5}	0.9896	4.9

The kinetic adsorption results of pseudo-second and pseudo-first-order kinetic models are shown in Figures 10 and 11, and the corresponding kinetic parameters are summarized in Table 2. The kinetic processes for the adsorption of Pb^{2+} ions on the HCPMs, CPMs and HAP powders follow pseudo-first-order and pseudo-second-order kinetic models. For the HCPMs, the correlation coefficients (R^2) of pseudo-first kinetic model and pseudo-second-order kinetic model are 0.9720~0.9873 and 0.9881~0.9993, respectively. For the CPMs, the correlation coefficients (R^2) of pseudo-first kinetic model and pseudo-second-order kinetic model are 0.9496~0.9948 and 0.9999, respectively. For the HAP powders, the correlation coefficients (R^2) of pseudo-first kinetic model and pseudo-second-order kinetic model are 0.9474~0.9889 and 0.9536~9896, respectively. The correlation coefficient (R^2) of the pseudo-second kinetic model is greater than the pseudo-first kinetic model, suggesting that the former exhibits better correlation coefficient than the latter for three samples and

under pH values of 2.5-7.0 (Table 2). The reason is attributed to the chemical adsorption of Pb^{2+} ions on the HCPMs, CPMs and HAP powders rather than simple physical adsorption. After adsorbing Pb^{2+} ions on above three samples, rod-like PbHAP and plate-like CS-Pb are formed (Figures 3-6).

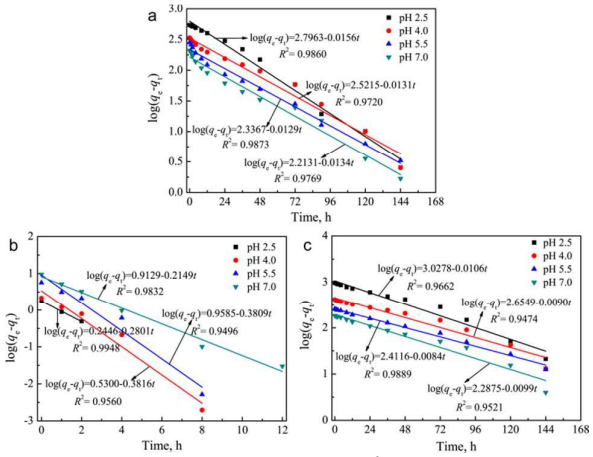

Figure 10. Pseudo-first-order rate simulation of Pb^{2+} adsorption on different samples under the lead solutions with a concentration of 400 mg/L: (a) HCPMs; (b) CPMs; (c) HAP powders.

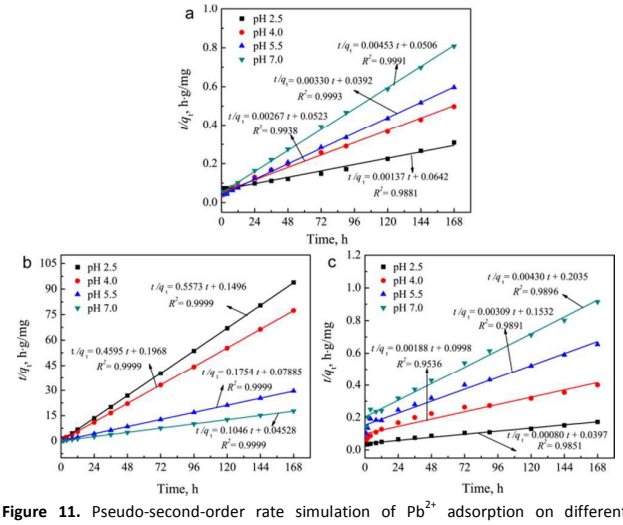

Figure 11. Pseudo-second-order rate simulation of Pb^{2+} adsorption on different samples under the lead solutions with a concentration of 400 mg/L: (a) HCPMs; (b) CPMs; (c) HAP powders.

The initial adsorption rates (h_i) of Pb^{2+} ions on the HCPMs, CPMs and HAP powders are calculated according to pseudo-second-order kinetic model (Table 2). The CPMs can chemically adsorb Pb^{2+} ions via the chemical bond of $-NH_2$ groups with Pb^{2+} ions. The protonation degree of $-NH_2$ groups decreases with the increase of pH value from 4.0 to 7.0, resulting in the increase of initial adsorption rates from 5.1 to 22.1 $mg \cdot g^{-1} \cdot h^{-1}$. Notably, the initial adsorption rate (6.7 $mg \cdot g^{-1} \cdot h^{-1}$) at the pH value of 2.5 is greater than that at pH=4.0, suggesting that the ion exchange reaction of H^+ ions in NH_4^+ by Pb^{2+} ions plays an important role in chemically adsorbing Pb^{2+} ions (Table 2). HAP powders can be dissolved in acid solutions, and the released PO_4^{3-} ions react with Pb^{2+} ions to form PbHAP rods. As the pH values of solutions decrease from 7.0 to 2.5, more PO_4^{3-} ions are released from the HAP powders, and thus the corresponding initial adsorption rates increase from 4.9 to 25.2 $mg \cdot g^{-1} \cdot h^{-1}$ (Table 2). The HCPMs exhibit the great initial adsorption rates for Pb^{2+} range from 15.6-25.5 $mg \cdot g^{-1} \cdot h^{-1}$ under the pH values of 2.5-7.0 because both the HAP and CS have cooperative adsorption for heavy metal ions (Table 2).

Table 2 indicates that the adsorption rate constants (k_2) of Pb^{2+} ions on the HCPMs, CPMs and HAP powders are 2.92×10^{-5}~4.06×10^{-4}, 1.8~9.6 and 1.61×10^{-5}~9.09×10^{-5} $mg \cdot g^{-1} \cdot h^{-1}$, respectively. CS adsorbs Pb^{2+} ions in lead solutions by the complexation reaction to form CS-Pb complex, while HAP chemically adsorbs Pb^{2+} ions mainly by the conversion reaction of HAP to PbHAP (Figure 4). With increasing the adsorption time, the as-formed PbHAP rods may block the diffusion of PO_4^{3-} ions from the HAP particles, and thus decrease the adsorption rate of Pb^{2+} ions on the HCPMs or HAP powders. The above phenomenon does not take place in the adsorption process of Pb^{2+} ions on the CPMs because few CS-Pb complex is formed (Figure 6). Therefore, three samples have different initial adsorption rate constants at pH=2.0~7.0, and the order is as follow: CPMs > HCPMs > HAP powders.

3.5 Effect of Pb^{2+} ion concentrations on adsorption performance of HCPMs

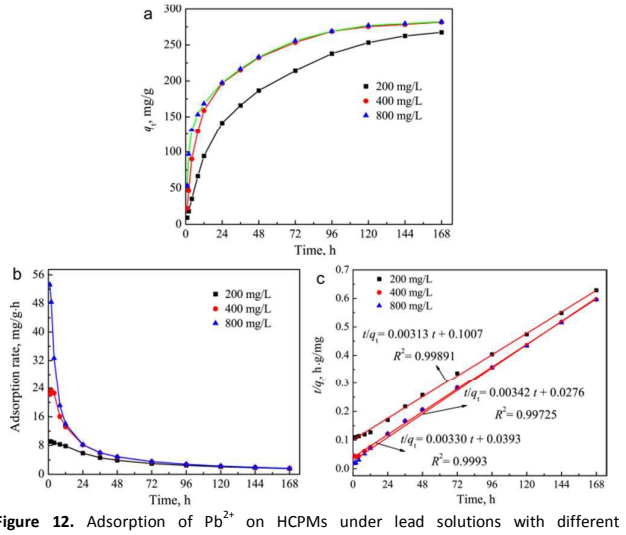

Figure 12. Adsorption of Pb^{2+} on HCPMs under lead solutions with different concentrations: (a) cumulative adsorption amounts; (b) adsorption rates at different time; and (c) pseudo-second-order rate simulation.

In order to investigate the effects of lead solution concentrations on cumulative adsorption amounts, adsorption rates of Pb^{2+} ions on HCPMs, the Pb^{2+} ions solutions with different concentrations of 200, 400 and 800 mg/L are flowed through the adsorbents. For three solutions at pH=5.5, the HCPMs possess similar adsorption trends. The experimental equilibrium adsorption amounts of the HCPMs under the Pb^{2+} ion solutions with concentrations of 200, 400 and 800 mg/L are 267.4, 281.7 and 282.1 mg/g, respectively. As we know, the whole adsorption process of Pb^{2+} ions on adsorbents can

be divided into two steps including: (i) the diffusion of Pb^{2+} ions from lead solutions to adsorbent surfaces; and (ii) the chemical (or physical) adsorption of Pb^{2+} ions on adsorbents. The high Pb^{2+} ion concentrations improve the concentration gradient from the lead solutions to the adsorbent surfaces, and thus increase the diffusion rate of Pb^{2+} ions. Under the low Pb^{2+} ion concentrations of 200-400 mg/L, the whole adsorption rate is determined by the diffusion rate of Pb^{2+} ions. Therefore, the HCPMs have greater adsorption amounts under the Pb^{2+} ion concentration of 400 mg/L at different time ranging from 0 to 168 h than under the Pb^{2+} ion concentration of 200 mg/L, (Figure 12a). Notably, if the Pb^{2+} ion concentration increases from 400 to 800 mg/L, the whole adsorption rate is determined by the chemical (or physical) adsorption of Pb^{2+} ions on adsorbents rather than the diffusion rate of Pb^{2+} ions. There are similar chemical (or physical) adsorption rates under the Pb^{2+} ion concentration of 400 and 800 mg/L, so two adsorption curves almost overlap (Figure 12a).

The adsorption rates of Pb^{2+} ions on the HCPMs decrease with time under the different concentrations of lead solutions (Figure 12b), because the consumption amounts of the HAP and CS in the adsorbents increase by the formation of PbHAP rods and CS-Pb complex (Figure 4). In the initial stage, there are enough HAP and CS to adsorb Pb^{2+} ions, so the initial adsorption rates depend mainly on the concentrations of Pb^{2+} ions. A high initial Pb^{2+} concentration may improve the concentration gradient from the lead solution to the adsorbent surface, and thus increase the diffusion rate of Pb^{2+} ions. Therefore, with increasing the concentrations of Pb^{2+} ions, the initial adsorption rates (h_i) of Pb^{2+} ions on HCPMs increase, too. The initial adsorption rates are 9.93, 25.45 and 36.27 $mg \cdot g^{-1} \cdot h^{-1}$ under the lead solution with the concentrations of 200, 400 and 800 mg/L, respectively. Figure 12c shows the pseudo-second-order rate simulation of Pb^{2+} ions on the HCPMs for the different concentrations. For three curves, the correlation coefficients are all over 0.99, suggesting that all adsorption curves are in good agreement with pseudo-second-order kinetic model.

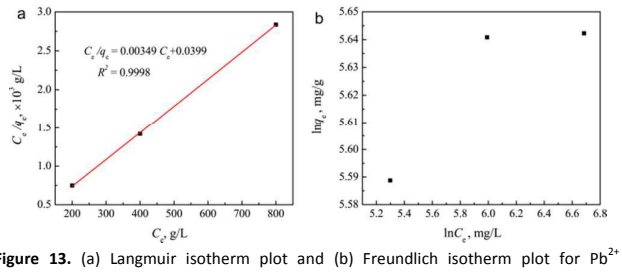

Figure 13. (a) Langmuir isotherm plot and (b) Freundlich isotherm plot for Pb^{2+} adsorption on HCPMs.

The equilibrium adsorption isotherms are of fundamental importance in the design of adsorptive systems. In the present work, the adsorption isotherm for the adsorbed Pb^{2+} ions on the HCPMs are analyzed by Langmuir and Freumdlich isotherm models.[75,76] The linear form of Langmuir isotherm model is given by Eq. (8):[75]

$$\frac{C_e}{q_e} = \frac{1}{K_e q_{max}} + \frac{C_e}{q_{max}} \quad (8)$$

where q_{max} ($mg \cdot g^{-1}$) is the maximum adsorption capacity, q_e ($mg \cdot g^{-1}$) is the equilibrium adsorption amount in adsorbed phases, C_e (mg/L) is the equilibrium concentration of metal ions in liquid phases, and K_e (l/g) is the Langmuir constant, which is related to the binding energy of Pb^{2+} ions to active site.

Freundlich isotherm model can be expressed as the following equation:[76]

$$\ln q_e = \ln K_f + \frac{1}{n} \ln C_e \quad (9)$$

where K_f is roughly an indicator of the adsorption capacity and $1/n$ is the adsorption intensity. The magnitude of the exponent $1/n$ gives an indication of the favorability of adsorption. The value of $1/n$ is more than 1, which represents favorable adsorption condition.

Figure 13a shows that the value of correlation coefficient for the adsorption of Pb^{2+} on the HCPMs is 0.9998, which demonstrates the good fitting of experimental data by Langmuir isotherm model. The Langmuir constant is 87.5 l/g, suggesting that the HCPMs have good adsorption affinity for Pb^{2+} ions since the Langmuir constant is proportional to the binding energy. The cumulative maximum adsorption capacity of HCPMs for absorbing Pb^{2+} ions is considered as 286.5 mg/g (Figure 13a), which is similar to their experimental equilibrium adsorption amounts under the Pb^{2+} ion concentrations of 400 and 800 mg/L. The Freundlich isotherm is also employed to explain the adsorption of Pb^{2+} on the HCPMs. However, the plot $\ln q_e$ versus $\ln C_e$ do not exhibit linear relationship (Figure 13b), suggesting that the adsorption process do not obeys Freundlich isotherm model.

4. Conclusions

In summary, HCPMs have been fabricated according to the following steps: (i) freeze-drying fabrication of BCPMs; and (ii) formation of HCPMs from BCPMs by NaOH solution treatment. The HCPMs possess the interconnected 3D macropores with a pore size of 150-240 μm and a porosity of 93.0%, which provide the channels for the flow of Pb^{2+} solutions. The nano-HAP rods with a length of 500 nm and a diameter of ~20 nm are dispersed uniformly within the porous materials. The lead adsorption experimental suggests that the HCPMs exhibit good adsorption property for Pb^{2+} ions. With decreasing pH values of lead solutions from 7.0 to 2.5, the experimental equilibrium adsorption amounts increase from 208.0 to 548.9 mg/g. The good adsorption property of the HCPMs is attributed to the formation of PbHAP and CS-Pb complex after adsorbing Pb^{2+} ions. The adsorption curve of Pb^{2+} ions on the HCPMs exhibits good compliance with pseudo-second-order kinetic and Langmuir isotherm model. Based on Langmuir isotherm mode, the maximum adsorption capacity of HCPMs for absorbing Pb^{2+} ions arrives at 286.5 mg/g when the pH value is kept at 5.5.

Hence, the HCPMs have great applications for removal of Pb^{2+} ions from environmental and industrial wastes.

Acknowledgements

This research was supported by Natural Science Foundation of China (No. 51372152), Program of Shanghai Normal University (Nos. DZL124, DCL201303, SK201333), Innovation Foundation of Shanghai Education Committee (No. 14ZZ124), and Baosteel Development Co., Ltd..

Notes and references

1 Y. C. Lu, J. He and G. S. Luo, *Chem. Eng. J.*, 2013, **226**, 271.
2 G. Hu, J. Li and G.M. Zeng, *J. Hazard. Mater.*, 2013, **261**, 470.
3 D. G. Liu, Z. H. Li, W. Li, Z. R. Zhong, J. Q. Xu, J. J. Ren and Z. S. Ma, *Ind. Eng. Chem. Res.*, 2013, **52**, 11036.
4 J. G. Pounds, G. J. Long and J. F. Rosent, *Environ. Health Persp.*, 1991, **91**, 17.
5 G. Gyananath and D.K. Balhal, *Cell. Chem. Technol.*, 2012, **46**, 121.
6 Y. W. Fen, W. M. M. Yunus and Z. A. Talib, *Optik*, 2013, **124**, 126.
7 S. Saber-Samandari, S. Saber-Samandar, N. Nezafati and K. Yahya, *J. Environ. Manage.*, 2014, **146**, 481.
8 M. Aliabadi, M. Irani, J. Ismaeili and S. Najafzadeh, *J. Taiwan. Inst. Chem. Eng.*, 2014, **45**, 518.
9 N. Bensacia, I. Fechete, S. Moulay, O. Hulea, A. Boos and F. Garin, *C. R. Chimie.*, 2014, **17**, 869.
10 A. S. Özcan, Ö. Gök and A. Özcan, *J. Hazard. Mater.*, 2009, **161**, 499.
11 B. Kizilkaya and A. A. Tekınay, *J. Chem.*, 2014, **2014**, 1.
12 Y. C. Chang, S. W. Chang and D. H. Chen, *React. Funct. Polym.*, 2006, **66**, 335.
13 X. F. Sun, C. Y. Liu, Y. Ma, S. G. Wang, B. Y. Gao and X. M. Li, *Colloid. Surf. B*, 2011, **82**, 456.
14 S. P. Wu, J. Hu, L. T. Wei, Y. M. Du, X. W. Shi, H. B. Deng and L. Zhang, *J. Environ. Chem. Eng.*, 2014, **2**, 1568.
15 C. T. Benatti, C. R. G. Tavares and E. Lenzi, *J. Environ. Manage.*, 2009, **90**, 504.
16 S. Kadouche, H. Zemmouri, K. Benaoumeur, N. Drouiche, P. Sharrock, H. Lounici and M. O. Mecherri, *Proced. Eng.*, 2012, **33**, 377.
17 L. M. Cui, L. H. Hu, X. Y. Guo, Y. K. Zhang, Y. G. Wang, Q. Wei and B. Du, *J. Mol. Liq.*, 2014, **198**, 157.
18 R. Donat, A. Akdogan, E. Erdem and H. Cetisli, *J. Colloid. Interf. Sci.*, 2005, **286**, 43.
19 L. M. Cui, W. Y. Xu, X. Y. Guo, Y. K. Zhang, Q. Wei and B. Du, *J. Mol. Liq.*, 2014, **197**, 40.
20 H. L. Lu, W. H. Zhang, Y. X. Yang, X. F. Huang, S. Z. Wang and R. L. Qiu, *Water Res.*, 2012, **46**, 854.
21 R. Sitko, P. Janik, B. Feist, E. Talik and A. Gagor, *ACS Appl. Mater. Inter.*, 2014, **6**, 20144.
22 F. Zhang, Z. S. Zhao, R. Q. Tan, W. Xu, G. B. Jiang and W. J. Song, *Chem. Eng. J.,* 2012, **203**, 110.
23 M. Rafatullah, O. Sulaiman, R. Hashim and A. Ahmad, *Wood Sci. Technol.,* 2012, **46**, 221.
24 F. J. Zhang, X. X. Qu, S. Chen and C. Q. Ran, *Front. Environ. Sci. Eng.*, 2012, **6**, 484.
25 Y. H. Zhan, J. W. Lin and J. Li, *Environ. Sci. Pollut. Res.*, 2013, **20**, 2512.
26 S. Hokkanen, E. Repo, L. J. Westholm, S. Lou, T. Sainio and M. Sillanpää, *Chem. Eng. J.*, 2014, **252**, 64.
27 A. Xenidis, C. Stouraiti and N. Papassiopi, *J. Hazard. Mater.*, 2010, **177**, 929.
28 N. S. Pai and S. K. Yen, *Int. J. Hydrog. Energy.*, 2013, **38**, 13249.
29 D. P. Minh, N. D. Tran, A. Nzihou and P. Sharrock, *Chem. Eng. J.,* 2013, **232**, 128.
30 Y. P. Xu, F. W. Schwartz and S. J. Traina, *Environ. Sci. Technol.*, 1994, **28**, 1472.
31 M. Srinivasan, C. Ferraris and T. White, *Environ. Sci. Technol.*, 2006, **40**, 7054.
32 D. P. Minh, N. D. Tran, A. Nzihou and P. Sharrock, *Chem. Eng. J.*, 2014, **243**, 280.
33 M. Peld, K. Tõnsuaadu and V. Bender, *Environ. Sci. Technol.*, 2004, **38**, 5626.
34 Y. Lei, J. J. Guan, W. Chen, Q. F. Ke, C. Q. Zhang and Y. P. Guo, *RSC Adv.*, 2015, **5**, 25462.
35 X. Y. Zhao, Y. J. Zhu, J. Zhao, B. Q. Lu, F. Chen, C. Qi and J. Wu, *J. Colloid. Interf. Sci.,* 2014, **416**, 11.
36 M. J. Olszta, X. Chemg, S. S. Jee, R. Kumar, Y. Y. Kim, M. J. Kaufman, E. P. Douglas and L. B. Gowder, *Mater. Sci. Eng. R*, 2007, **58**, 77.
37 J. Chen, Y. Wang and X. Chen, *J Biomat. Sci.-Polym. E.*, 2009, **20**, 1555.
38 J. Chen, K. Nan, S. Yin, Y. Wang, T. Wu and Q. Zhang, *Colloid. Surface. B*, 2010, **81**, 640.
39 J. Chen, Q. Yu, G. Zhang, S. Yang, J. Wu and Q. Zhang, *Colloid. Surface. B*, 2012, **93**, 100.
40 J. Yang, T. Long, N. F. He, Y. P. Guo, Z. A. Zhu and Q. F. Ke, *J. Mater. Chem. B.*, 2014, **2**, 6611.
41 S. E. Baker, P. E. Colavita, K. Y. Tse and R. J. Hamers, *Chem. Mater.*, 2006, **18**, 4415.
42 G. Lawrie, I. Keen, B. Drew, A. Chandler-Temple, L. Rintoul, P. Fredericks and L. Grondahl, *Biomacromolecules*, 2007, **8**, 2533.
43 L. Jin and R.B. Bai, *Langmuir*, 2002, **18**, 9765.
44 M. R. Gandhi and S. Meenakshi, *J. Hazard. Mater.*, 2012, **203-204**, 29.
45 G. Z. Kyzas, P. I. Siafaka, E. G. Pavlidou, K. J. Chrissafis and D. N. Bikiaris, *Chem. Eng. J.*, 2015, **259**, 438.
46 J. J. Li, D. W. Zhu, J. W. Yin, Y. X. Liu, F. L. Yao and K. D. Yao, *Mater. Sci. Eng. C.*, 2010, **30**, 795.
47 T. C. Coelho, R. Laus, A. S. Mangrich, V. T. deFávere and M. C. M. Laranjeira, *React. Funct. Polym.*, 2007, **67**, 468.
48 L. E. Abugoch, C. Tapia, M. C. Villamán, M. Yazdani-Pedram and M. Díaz-Dosque, *Food Hydrocolloid.*, 2011, **25**, 879.
49 W. Chen, T. Long, Y. J. Guo, Z. A. Zhu and Y.P. Guo, 9*J. Mater. Chem. B.*, 2001, **22**, 1205.
50 D. Walsh, T. Furuzono and J. Tanaka, *Biomaterials*, 2001, **22**, 1205.
51 F. Ye, H.F. Guo, H. J. Zhang and X. He, *Acta Biomater*., 2010, **6**, 2212.
52 B. Sandrine, N. Ange, B. A. Didier, C. Eric and S. Patrick, *J. Hazard. Mater.*, 2007, **139**, 443.
53 Z. Z. Zhang, M. Y. Li, W. Chen, S. Z. Zhu, N. N. Liu and L. Y. Zhu, *Environ. Pollut*., 2010, **158**, 514.
54 S. H. Jang, Y. G. Jeong, B. G. Min, W. S. Lyoo and S. C. Lee, *J. Hazard. Mater.*, 2008, **159**, 294.
55 S. H. Jang, B. G. Min, Y. G. Jeong, W. S. Lyoo and S. C. Lee, *J. Hazard. Mater.*, 2008, **152**, 1285.
56 F. Zhuang, R. Tan, W. Shen, X. Zhang, W. Xu and W. Song, *J. Alloy. Compd.*, 2015, **637**, 531.
57 G. Fahimeh, M. Ahmad and E. Rahmatollah, *Chem. Eng. J.*, 2012, **200-202**, 471.
58 Y. C. Lu, J. He and G. Luo, *Chem. Eng. J.*, 2013, **226**, 271.
59 R. Rusmin, B. Sarkar, Y. Liu, S. McClure and R. Naidu, *Appl. Surf. Sci.*, 2015, **353**, 363.
60 H. V. Tran, L. D. Tran and T. N. Nguyen, *Mater. Sci. Eng. C*, 2012, **30**, 304.
61 W. S. Wan Ngah and S. Fatinathan, *J. Environ. Manage.*, 2010, **91**, 958.

62 L. Chu, C. Liu, G. Zhou, R. Xu, Y. Tang, Z. Zeng and S. Luo, *J. Hazard. Mater.,* 2015, **300**, 153.
63 M. Yurtsever and I. A. Sengil, *J. Hazard. Mater.*, 2009, **163**, 58.
64 M. M. Rao, D. K. Ramana, K. Seshaiah, M. C. Wang and C. S. W. Chang, *J. Hazard. Mater.*, 2009, **166**, 1006.
65 A. Afkhami, M. Saber-Tehrani and H. Bagheri, *J. Hazard. Mater.*, 2010, **181**, 836.
66 G. N. Manju, K. A. Krishnan, V. P. Vinod and T. S. Anirudhan, *J. Hazard. Mater.*, 2002, **91**, 221.
67 Y. M. Zhoua, S. Y. Fua, L. L. Zhang, H. Y. Zhan and M. V. Levit, *Carbohyd. Polym.*, 2014, **101**, 75.
68 F. Xu, N. Zhang, Y. Long, Y. Si, Y. Liu, X. Mi, X. Wang, F. Xing, X. You and J. Gao, *J. Hazard. Mater.*, 2011, **188**, 148.
69 J. R. Rangel-Mendez, R. Monroy-Zepeda, E. Leyva-Ramos, P. E. Diaz-Flores and K. Shirai, *J. Hazard. Mater.*, 2009, **162**, 503.
70 H. Xu, L. Yang, P. Wang, Y. Liu and M. Peng, *J. Environ. Manage.*, 2008, **86**, 319.
71 M. V. Jadhav and Y. S. Mahajan, *World Rev. Sci. Technol. Sust. Develop.*, 2011, **8**, 276.
72 F. Googerdchian, A. Moheb and R. Emadi, *Chem. Eng. J.*, 2012, **200**, 471.
73 M. Aliabadi, M. Irani, J. Ismaeili, H. Piri and M. J. Parnian, *Chem. Eng. J.*, 2013, **220**, 237.
74 K. Y. Shin, J. Y. Hong and J. Jang, *J. Hazard. Mater.*, 2011, **190**, 36.
75 Y. Feng, J. -L. Gong, G. -M. Zeng, Q. -Y. Niu, H. -Y. Zhang, C. -G. Niu, J. -H. Deng and M. Yan, *Chem. Eng. J.,* 2010, **162**, 487.
76 W. Zheng, X. M. Li, Q. Yang, G. M. Zeng, X. X. Shen, Y. Zhang and J. J. Liu, *J. Hazard. Mater.*, 2007, **147**, 534.

Graphical Abstract

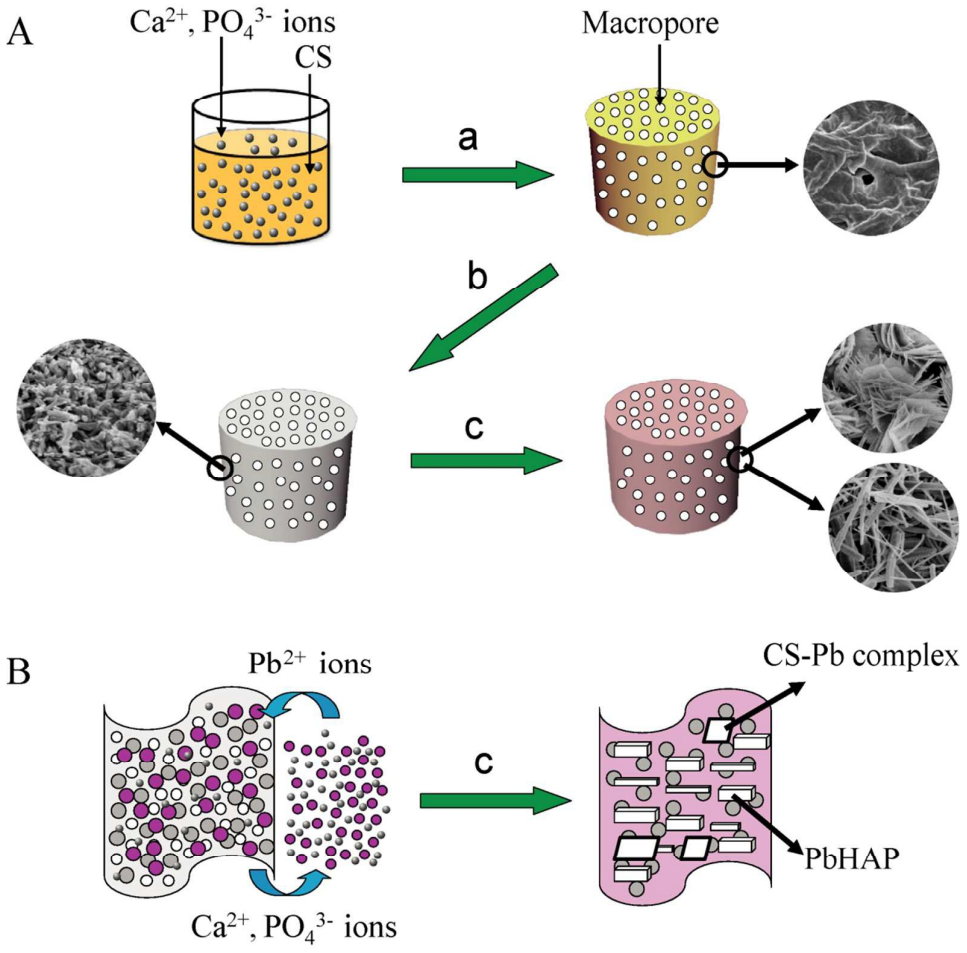

Nano-hydroxyapatite/chitosan porous materials possess great applications for removal of Pb^{2+} ions from environmental and industrial wastes.